

# Programmable array antenna based on nematic liquid crystals for the Ka-band

WANG Qiang<sup>1,2</sup>, KE Junchen<sup>1,2</sup>, BAI Lin<sup>3</sup>

(1. Guangxi Key Laboratory of Optoelectronic Information Processing, Guilin University of Electronic Technology, Guilin 541004, China; 2. School of Optoelectronic Engineering, Guilin University of Electronic Technology, Guilin 541004, China; 3. School of Information Science and Engineering, Southeast University, Nanjing 211189, China)

**Abstract:** A programmable low-profile array antenna based on nematic liquid crystals (NLCs) is proposed. Each antenna unit comprises a square patch radiating structure and a tunable NLC-based phase shifter capable of achieving a phase shift exceeding  $360^\circ$  with high linearity. First, the above 64 antenna units are periodically arranged into an  $8 \times 8$  NLC-based antenna array, and the bias voltage of the NLC-based phase shifter loaded on the antenna unit is adjusted through the control of the field-programmable gate array (FPGA) programming sequences. This configuration enables precise phase changes for all 64 channels. Numerical simulation, sample processing, and experimental measurements of the antenna array are conducted to validate the performance of the antenna. The numerical and experimental results demonstrate that the proposed antenna performs well within the frequency range of 19.5-20.5 GHz, with a 3 dB relative bandwidth of 10% and a maximum main lobe gain of 14.1 dBi. A maximum scanning angle of  $\pm 34^\circ$  is achieved through the adjustment of the FPGA programming sequence. This NLC-based programmable array antenna shows promising potential for applications in satellite communication.

**Key words:** array antenna; nematic liquid crystals; electronically beam scanning; field programmable gate array (FPGA)

DOI:10.3969/j.issn.1003-7985.2025.01.010

Wireless communication systems are indispensable in the information age<sup>[1-7]</sup>. The rapid advancement of wireless communication technology requires continuous improvements in antenna performance across mul-

multiple dimensions. According to the 6G white paper<sup>[8]</sup>, high-frequency operation and beam-scanning are key visions for future wireless communication systems. Currently, beam-scanning can be achieved through various technologies, including microelectromechanical systems<sup>[9-10]</sup>, pin diodes<sup>[11-12]</sup>, and varactors<sup>[13-14]</sup>. However, owing to processing limitations and parasitic effects, tunable devices based on conventional semiconductor components operating in the microwave frequency band face challenges in maintaining performance at higher frequencies. To address these challenges in the millimeter-wave (mmW) bands, researchers are exploring novel phase-shifting techniques based on the unique properties of various materials, including liquid crystals, graphene, and  $\text{VO}_2$ <sup>[15-17]</sup>. Notably, nematic liquid crystals (NLCs) exhibit a distinct response to electromagnetic (EM) waves in the mmW frequency band, offering advantages such as low loss and ease of integration. Studies have shown that array antennas incorporating NLC materials facilitate dynamic regulation of high-frequency EM waves<sup>[18-19]</sup>. However, the electromagnetic properties of these NLC-based devices are often controlled through the manual adjustment of the bias voltage applied to the NLCs, which restricts the advancement of the devices toward intelligent and autonomous operation.

This study presents the design, fabrication, and evaluation of an  $8 \times 8$  NLC-based Ka-band programmable phased-array antenna. The NLC-based phase shifter in each antenna unit plays a critical role in enabling dynamic regulation. Additionally, a 64-channel adjustable power supply module, controlled by a field-programmable gate array (FPGA)<sup>[20]</sup>, has been developed to provide independently controllable bias voltages to each NLC-based phase shifter unit. By loading different coding sequence streams into the FPGA, the 64 output channels apply distinct voltages to the NLC-based phase shifters, thereby achieving beam-scanning functionality. Experimental results demonstrate that when different coding sequences are loaded into the FPGA, the antenna beam can be scanned from  $-34^\circ$  to  $34^\circ$ . Within the frequency range of 19.5-20.5 GHz, the antenna achieves a 3 dB relative bandwidth of 10% and a maximum main lobe gain of 14.1 dBi. These experimental findings closely align

Received 2024-10-25, Revised 2024-12-11.

**Biographies:** Wang Qiang (1991—), male, doctor, associate professor; Ke Junchen (corresponding author), male, doctor, kejunchenddyb@foxmail.com.

**Foundation items:** The National Natural Science Foundation of China (No. 62401168, 62401139, 62401170), China Postdoctoral Science Foundation (No. 2023MD744197), Postdoctoral Fellowship Program of CPSF (No. GZC20230631), Project for Enhancing Young and Middle-aged Teacher's Research Basis Ability in Colleges of Guangxi (No. 2023KY0218), Guangxi Key Laboratory Foundation of Optoelectronic Information Processing (No. GD23102).

**Citation:** WANG Qiang, KE Junchen, BAI Lin. Programmable array antenna based on nematic liquid crystals for the Ka-band[J]. Journal of Southeast University (English Edition), 2025, 41 (1): 78-83. DOI: 10.3969/j.issn.1003-7985.2025.01.010.

with numerical simulations, validating the proposed design. The concept of the NLC-based programmable array antenna shows potential for future application in low-Earth-orbit (LEO) satellite ground station terminals.

## 1 Antenna Design

### 1.1 Design of antenna unit based on NLCs

To implement the proposed programmable array antenna, as illustrated in Fig. 1(a), we first design an NLC-based antenna unit capable of achieving full-phase ( $2\pi$ ) coverage. As illustrated in Fig. 1(b), the antenna unit comprises a multilayer structure with six layers: upper metal, upper substrate, middle metal, NLCs, bottom metal, and bottom substrate. The operational principle involves coupling the EM wave signal from the power divider network on the upper glass substrate to the NLC-based phase shifter through a slot. The signal is then coupled to the radiation patch on the upper glass substrate through another slot, where it radi-

ates as EM waves. This coupling structure is designed to effectively minimize the size of the array antenna while simultaneously preventing crosstalk between radio frequency and direct current (DC) signals. The radiation patch is square, with a side length of 2.8 mm. The dielectric constant of the NLC material varies from 2.4 to 3.2 under the application of a tunable DC voltage, with a tangent loss of 0.005 at 20 GHz. The radiation patches, metal ground, power divider, and phase shifter are photoetched on a silicon glass (BF33) substrate, which has a permittivity of 4.55 and a loss tangent of 0.001 in the operating Ka-band. The radiation patch is fed via coupling slot 1, which has dimensions  $L_a \times L_b = 1.5 \text{ mm} \times 0.6 \text{ mm}$ . The thicknesses of the silicon glass dielectric substrate, NLC material layer, and metal copper are  $H_s = 0.7 \text{ mm}$ ,  $H_{LC} = 0.07 \text{ mm}$ , and  $t = 0.002 \text{ mm}$ , respectively. Notably, the metal thickness is five times the skin depth at the designed frequency, which ensures that electromagnetic waves cannot penetrate the metal.

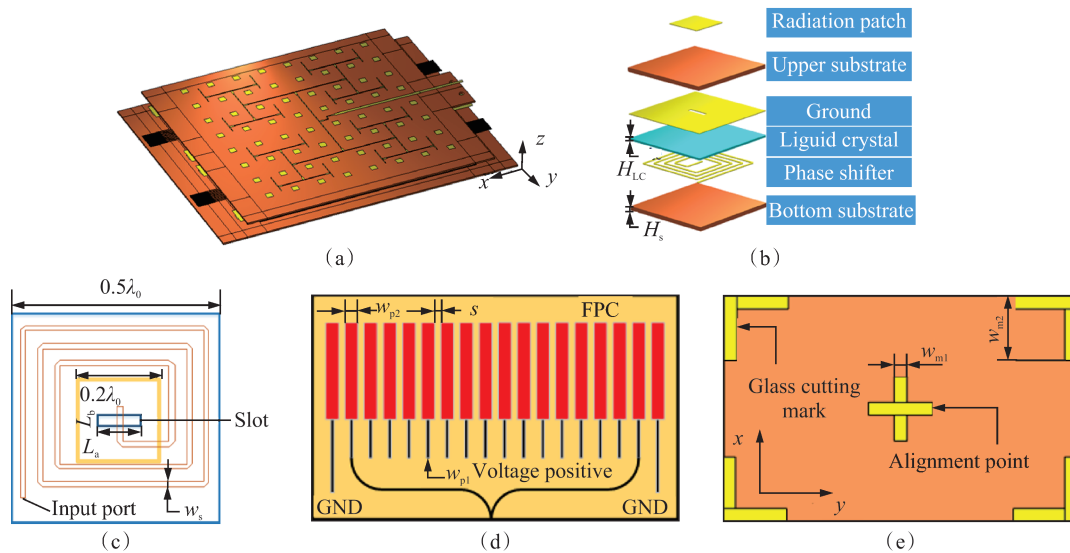


**Fig. 1** Schematic of the proposed programmable array antenna. (a) 3D view of the programmable array antenna; (b) Geometry of the designed antenna unit based on NLCs; (c) Tunable phase shifter with a spiral structure; (d) FPGA-controlled DC bias circuits; (e) Alignment points indicating placement coordinates and angles for device processing

The core component of the antenna unit is the NLC-based phase shifter, which features a compact spiral structure etched onto the upper surface of the bottom substrate, as illustrated in Fig. 1(c). This design minimizes space usage. The NLC-based phase shifter provides a continuous phase shift ranging from  $0^\circ$  to  $360^\circ$  at 20 GHz, with an insertion loss of 2.8 dB and a return loss below 12 dB. The input impedance is set at  $50 \Omega$ , and the line width is defined as  $w_s = 0.2 \text{ mm}$ . The phase shift can be calculated accurately using theoretical values of NLC properties and transmission line theory. The relationship between the calculated phase change  $\Delta\phi$  and the dielectric constant  $\epsilon$  of the NLC is expressed by the following formula:

$$\Delta\phi = \frac{2\pi l}{\lambda_0} (\sqrt{\epsilon_{\parallel}} - \sqrt{\epsilon_{\perp}}) \quad (1)$$

where  $\lambda_0$  is the wavelength of the electromagnetic wave in a vacuum, and  $l$  is the length of the spiral structure of the microstrip transmission line. A bias voltage  $V$  is applied between the metal patch and the ground to generate the bias E-field. The axial direction  $\mathbf{n}$  of the NLC molecules can be altered by changes in the external environment, such as temperature, magnetic field, or electric field. Generally, when the bias voltage satisfies  $V \leq V_{th}$ , the long axis direction  $\mathbf{n}$  of the NLC molecule is perpendicular to the voltage direction, and the dielectric constant is denoted as  $\epsilon_{\perp}$ . When the bias voltage satisfies  $V \geq V_{SAT}$ , the long axis direction  $\mathbf{n}$  of the NLC molecule aligns with the voltage direction, and the dielectric con-

stant is denoted  $\epsilon_{\text{ril}}$ .  $V_{\text{th}}$  and  $V_{\text{SAT}}$  are the deflection threshold and saturation voltages of the NLC molecules, respectively. To avoid insufficient phase shift caused by machining errors, a 10% phase margin is included in the design length, resulting in a phase shift of approximately  $400^\circ$ . The total length  $l$  of the microstrip line is 90 mm. Note that the corners of the microstrip lines in the phase shifter are beveled to prevent unwanted reflections. In addition, the tested relationship between the relative permittivity (which ranges from 2.5 to 3.1) and the bias voltage is shown in Table 1. The desired relative permittivity, as indicated in previous simulations, can be achieved by adjusting the bias voltage. As illustrated in Figs. 1(d) and (e), the antenna and control circuit are connected via flexible printed circuit bonding. The 64-channel controller consists of an EP4CE15F17C8 FPGA chip and a 12-bit DAC module. This controller can generate a 30-Hz square-wave AC voltage signal ranging from 0 to 8 V, with a control precision of 2 mV.

**Table 1** Measured relative permittivity as a function of the driving voltage at 20 GHz

Driving voltage/V	4.5	5.0	5.5	6.0	6.5	7.0	7.5	8.0
Relative permittivity	2.51	2.55	2.64	2.82	2.95	3.08	3.12	3.15

The simulation of the designed NLC-based antenna unit is conducted using CST Microwave Studio software. After simulation and optimization, the performance of the antenna unit is illustrated in Fig. 2. As illustrated in Fig. 2(a), the reflection coefficient  $S_{11}$  of the antenna unit is below  $-10$  dB in the Ka-band, from 19.5 to 20.5 GHz. Fig. 2(b) illustrates the far-field characteristics of the designed antenna unit. As illustrated in Fig. 2(b), the radiation patterns of the E-plane and H-plane are nearly identical, which facilitates the subsequent implementation of circular polarization and beam scanning functions. The 3 dB beamwidth of the antenna unit is  $78^\circ$ , and the gain is 3 dB. The relative phase shift of the antenna unit exceeds  $360^\circ$ , as illustrated in Fig. 2(c).

## 1.2 Design of the array antenna

The detailed geometric configuration of the proposed programmable array antenna is illustrated in Fig. 1(a). It consists of a 64-element linear array arranged in 8 rows and 8 columns of antenna units. Additionally, the spacing between each antenna unit is half a wavelength, which helps to minimize the appearance of grating lobes.

To verify the impedance matching performance of the programmable NLC-based array antenna, the simulated and measured reflection coefficients are illustrated in Fig. 3. Good matching characteristics are observed, with  $S_{11}$  being less than  $-10$  dB across the Ka-band operating bandwidth, ranging from 19.5 to 20.5 GHz. It should also be noted that the measured  $S$ -parameter results are shifted toward lower frequencies compared with the simulated results, owing to errors introduced during the manufacturing process.

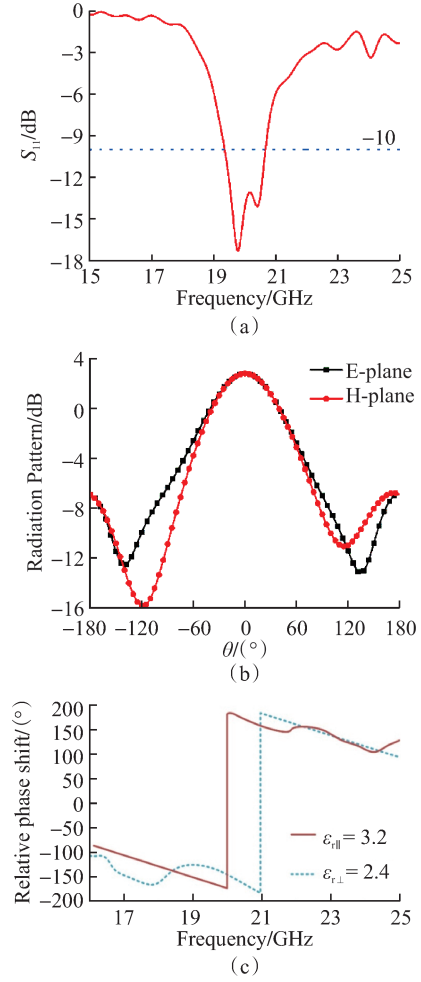


**Fig. 2** Simulated results of the designed NLC-based antenna unit. (a)  $S$ -parameter of the antenna unit; (b) Simulated 2D far-field radiation patterns of the E-plane and H-plane of the antenna unit at the center frequency of 20 GHz; (c) Relative phase shift of the antenna unit

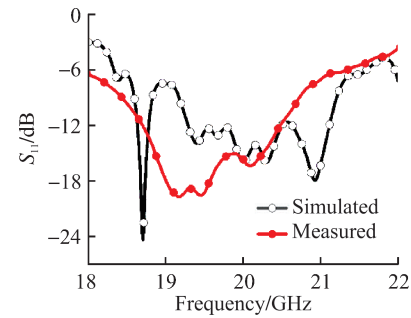


**Fig. 3** Simulated and measured  $S_{11}$  of the proposed programmable array antenna

## 1.3 Design of the bias voltage source with FPGA control circuit

Owing to the large number of units, manually adjusting and controlling the voltage across the NLC is no longer feasible. To achieve independent control of the antenna unit voltage in such a large-scale array, we use an FPGA control board to generate coding sequences. In this work, a 1 kHz square wave signal is used for bias control of the NLCs' dielectric constant, with the actual

bias voltage range being 0 to 5 V. The operating voltage of the FPGA ranges from 1.150 to 3.465 V, and it is powered by an AMS1117-3.3 chip in a TO-223 package. The AD8801 chip, functioning as a digital-to-analog converter (DAC), converts the digital coding sequence signals from the FPGA into analog signals for output. The analog devices AD8392 chip consists of four high-output

current, low-power operational amplifiers that amplify the 64-channel coding sequence signals output from the AD8801 chip. The schematic diagram of the entire system module is illustrated in Fig. 4. This module enables 0-30 V independently adjustable voltage and high-precision voltage regulation while ensuring 64 independent programmable feeders.

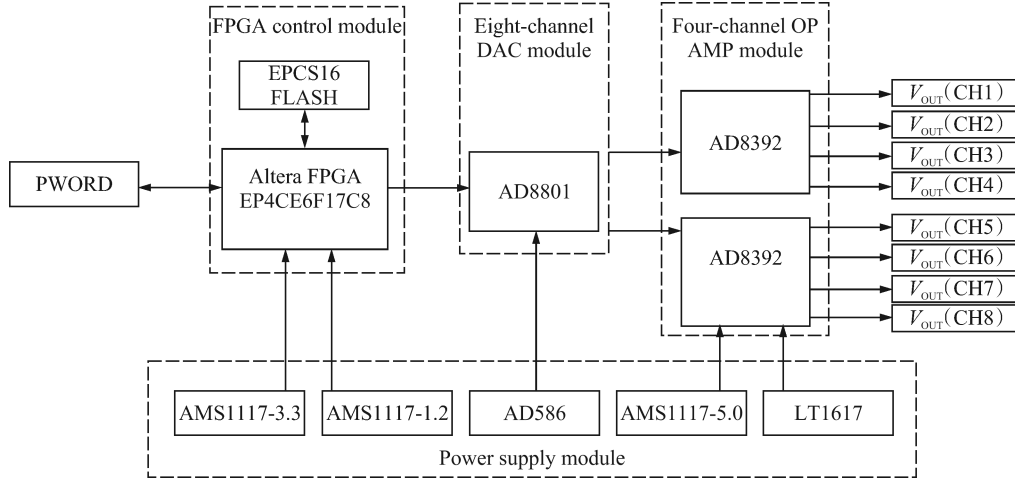


Fig. 4 Schematic of the 64-channel adjustable power module system

## 2 Experimental Results and Discussions

To further validate the proposed array antenna, we fabricate the array and measure its reflection coefficients and

radiation patterns. The photographs of the fabricated sample, the  $S$ -parameter measurement setup, the test scheme, and the far-field test environment are illustrated in Fig. 5.

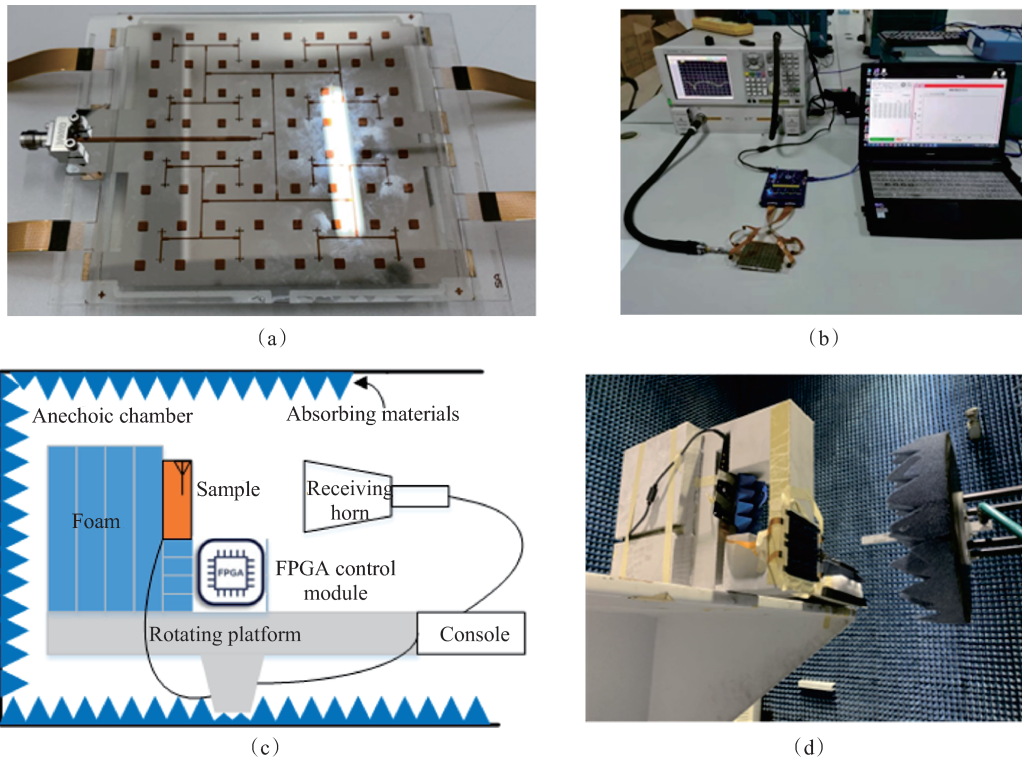


Fig. 5 Photographs of the fabricated sample and far-field experimental setup. (a) Top view of the sample; (b)  $S$ -parameter measurement setup; (c) Schematic diagram of the test scheme; (d) Photographs of the sample test in the anechoic chamber

We measure the far-field radiation patterns of the fabricated NLC array antenna in the anechoic chamber, as il-

lustrated in Fig. 5(d). The relationship between the calculated scanning angle  $\theta$  and the phase difference  $\Delta\phi$  is



given by the following formula:

$$\theta = \arcsin\left(\frac{\Delta\phi\lambda}{2\pi d}\right) \quad (2)$$

where  $\lambda$  is the wavelength of the vacuum EM wave,  $d$  is the distance between adjacent antenna units ( $0.5\lambda$ ), and  $\Delta\phi$  is the phase difference induced by the NLC.

The change in the dielectric constant of the NLC with voltage is simulated using numerical simulation software, and beam scanning from  $-34^\circ$  to  $34^\circ$  is theoretically achieved.

As illustrated in Fig. 6(a), the maximum antenna gain of the  $8 \times 8$  array antenna is 14.1 dB at 20 GHz, which is reduced by an insertion loss of approximately 3 dB due to the liquid crystal phase shifter. Compared with other high-precision adjustable phase shifters in the same frequency band, this loss is acceptable. Additionally, the array exhibits a sidelobe level of around  $-11.5$  dB and a cross-polarization of 15 dB. The simulation results for beam scanning are illustrated in Fig. 6(b), and the measured results for seven different voltage coding sequences

from the FPGA are illustrated in Fig. 6(c). As the FPGA controls the voltage magnitude applied to the NLC, the antenna main beam electronically scans from  $-34^\circ$  to  $34^\circ$ . A comparison of the simulation and experimental results reveals that when the beam is scanned at large angles, a significant grating lobe appears in the radiation pattern. The surface phase of the antenna array is tested in the near-field darkroom, and the measured scanning angles are in good agreement with the theoretically calculated values. The results of this study are compared with other programmable phased-array antennas based on liquid crystals in Table 2. The proposed programmable array antenna offers a more convenient approach for beam scanning while maintaining high performance.

**Table 2** Performance comparison with other studies

Reference	Radiation bandwidth/GHz	Maximum gain/dBi	Scanning coverage/( $^\circ$ )	Kind of antenna
Ref. [21]	22 to 26	20.2	$\pm 45$	Reflecting
Ref. [22]	30 to 40	6.7	$-22$ to $23$	Radiation
Ref. [23]	101 to 111	13.0	50	Reflecting
Current work	19 to 21	14.1	$-34$ to $34$	Radiation

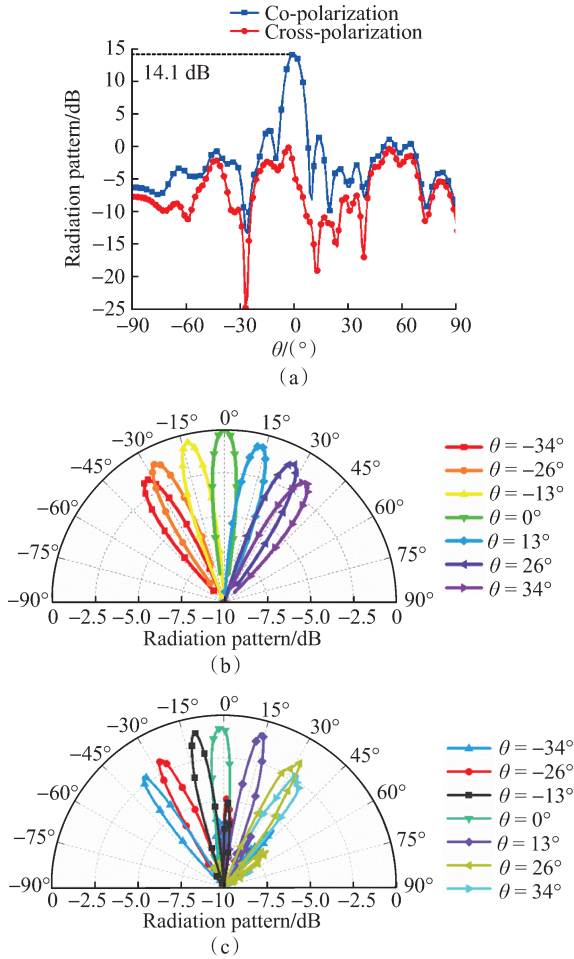


**Fig. 6** Simulated and measured radiation patterns of the proposed programmable array antenna at a central frequency of 20 GHz. (a) Gain and cross-polarization of the antenna array; (b) 2D simulated results under seven different coding sequences from the FPGA; (c) 2D measured results under seven different coding sequences from the FPGA

### 3 Conclusions

In this study, we present a low-cost, low-profile Ka-band programmable array antenna based on nematic liquid crystal, consisting of  $8 \times 8$  patch antenna units. We achieve electronic beam scanning control by adjusting the magnitude of the voltage applied across the NLC through an FPGA. The array antenna is experimentally validated for operation at the Ka-band satellite communication terminal downlink frequency of 20 GHz. Additionally, the antenna demonstrates excellent performance in continuous, accurate beam scanning from  $-34^\circ$  to  $34^\circ$  by adjusting the FPGA programming sequence. Through both theoretical design and experimental implementation, the proposed programmable array antenna is shown to maintain real-time beam scanning and support wireless communication with LEO satellites. This array antenna is expected to have wide applications in Ka-band LEO satellite communications.

### References

- [1] WU B, WU L, ZOU C R. Adaptive modulation in MIMO optical wireless communication systems[J]. Journal of Southeast University (English Edition), 2015, 31 (2): 175-180.
- [2] MIRANDA F A, SUBRAMANYAM G, VAN KEULS F W, et al. Design and development of ferroelectric tunable microwave components for Ku- and K-band satellite communication systems[J]. IEEE Transactions on Microwave Theory and Techniques, 2000, 48(7): 1181-1189.
- [3] YANG L L, QIN T, TU Y, et al. Simulation study on retinal imaging display based on meta-surface micro-nano structures[J]. Journal of Southeast University (Natural Science Edition), 2024, 54(4): 990-996. (in Chinese)

- [4] GU Y Q, CAO W Z, YUAN S F, et al. Inverse finite element method based shape reconstruction for spaceborne antenna structures under thermal load [J]. Journal of Southeast University (Natural Science Edition), 2024, 54(4): 997-1004. (in Chinese)
- [5] SHAO X X, HE X Y, ZHANG J L. Multi-scale two-dimensional digital image correlation system and its application [J]. Journal of Southeast University (Natural Science Edition), 2017, 47(2): 242-246. (in Chinese)
- [6] VALANARASI A, DHANASEKARAN R. Optimum band  $\varepsilon$  shaped miniature implantable antennas for telemetry applications [J]. IEEE Transactions on Antennas and Propagation, 2021, 69(1): 55-63.
- [7] ZHANG H, CHEN L Q, YANG B, et al. Secure lightweight data using scheme in 5G industrial Internet systems [J]. Journal of Southeast University (Natural Science Edition), 2024, 54(3): 772-780. (in Chinese)
- [8] WANG C X, YOU X H, GAO X Q, et al. On the road to 6G: Visions, requirements, key technologies, and testbeds [J]. IEEE Communications Surveys and Tutorials, 2023, 25(2): 905-974.
- [9] HUFF G H, BERNHARD J T. Integration of packaged RF MEMS switches with radiation pattern reconfigurable square spiral microstrip antennas [J]. IEEE Transactions on Antennas and Propagation, 2006, 54(2): 464-469.
- [10] RAJAGOPALAN H, RAHMAT-SAMII Y, IMBRIALE W A. RF MEMS actuated reconfigurable reflectarray patch-slot element [J]. IEEE Transactions on Antennas and Propagation, 2008, 56(12): 3689-3699.
- [11] ZHANG X G, JIANG W X, TIAN H W, et al. Pattern-reconfigurable planar array antenna characterized by digital coding method [J]. IEEE Transactions on Antennas and Propagation, 2020, 68(2): 1170-1175.
- [12] CHANG L, LI Y, ZHANG Z J, et al. Reconfigurable 2-bit fixed-frequency beam steering array based on microstrip line [J]. IEEE Transactions on Antennas and Propagation, 2018, 66(2): 683-691.
- [13] ZHANG X G, YU Q, JIANG W X, et al. Polarization-controlled dual-programmable metasurfaces [J]. Advanced Science, 2020, 7(11): 1903382.
- [14] BAI L, ZHANG X G, WANG Q, et al. Dual-band reconfigurable metasurface-assisted Fabry-Pérot antenna with high-gain radiation and low scattering [J]. IET Microwaves, Antennas & Propagation, 2020, 14 (15): 1933-1942.
- [15] JING H Y, TANG M R, HAN Y D, et al. Magnetic and microwave absorbing properties of M-type bariumferrite/graphene oxide composite microwave absorber [J]. Journal of Southeast University (English Edition), 2015, 31 (4): 511-515.
- [16] WANG Q, ZHANG X G, TIAN H W, et al. Millimeter-wave digital coding metasurfaces based on nematic liquid crystals [J]. Advanced Theory and Simulations, 2019, 2(12): 1900141.
- [17] LIU H W, CHEN Q C, SUN M Q, et al. Photoinduced dynamically tunable terahertz metamaterial absorber [J]. Journal of Southeast University (English Edition), 2024, 40(2): 148-154.
- [18] WANG Q, JIANG W X, SHEN H Y. Design of low-profile array antenna working at 110 GHz based on digital coding characterization [J]. Science China Information Sciences, 2021, 64(10): 209303.
- [19] KOMAR A, PANIAGUA-DOMÍNGUEZ R, MIROSHNICHENKO A, et al. Dynamic beam switching by liquid crystal tunable dielectric metasurfaces [J]. ACS Photonics, 2018, 5(5): 1742-1748.
- [20] MIAO P, WANG Z G. 10 Gbit/s PRBS tester implemented in FPGA [J]. Journal of Southeast University (English Edition), 2007, 23 (4): 516-519.
- [21] LI X Y, WAN Y L, LIU J, et al. Broadband electronically scanned reflectarray antenna with liquid crystals [J]. IEEE Antennas and Wireless Propagation Letters, 2021, 20(3): 396-400.
- [22] LI X Y, JIANG D, LIU J, et al. A Ka-band multilayer beaming-scanning antenna using liquid crystals [J]. IEEE Antennas and Wireless Propagation Letters, 2022, 21(1): 44-48.
- [23] LI J X, JIN T, ERNI D, et al. Design and numerical demonstration of a 2D millimeter-wave beam-scanning reflectarray based on liquid crystals and a static driving technique [J]. Journal of Physics D: Applied Physics, 2019, 52(27): 275103.

## 一种基于向列液晶的Ka频段可编程天线阵

王强<sup>1,2</sup>, 柯俊臣<sup>1,2</sup>, 柏林<sup>3</sup>

(1. 桂林电子科技大学广西光电信息处理重点实验室, 桂林 541004; 2. 桂林电子科技大学光电工程学院, 桂林 541004; 3. 东南大学信息科学与工程学院, 南京 211189)

**摘要:** 设计了一款基于向列液晶的可编程低剖面动态波束扫描阵列天线。该天线单元由方形的辐射贴片结构和向列液晶移相器组成, 其中移相器能够实现全相位 $360^\circ$ 线性变化。首先, 将上述64个液晶天线单元周期排列成 $8 \times 8$ 的阵列天线, 通过控制现场可编程门阵列(FPGA)编程编码序列来调节加载在天线单元中液晶移相器的电压, 并提供相应的相位变化, 从而对64路的液晶天线单元进行独立馈电控制。随后, 对该天线阵列进行了数值仿真、样品加工和实验测量。数值仿真和实验测量的结果表明, 该天线在19.5~20.5 GHz频率范围内具有良好的性能, 3 dB增益带宽为10%, 主瓣最大增益为14.1 dBi。通过控制FPGA的编码序列可实现 $\pm 34^\circ$ 的波束动态扫描。该向列液晶天线阵列在未来卫星通信领域具有潜在的应用价值。

**关键词:** 天线阵; 向列液晶; 电控波束扫描; 现场可编程门阵列(FPGA)

**中图分类号:** O441.4; TN929.5